Materials Today • Volume 71 • December 2023

A New Ternary Co-Free Layered Cathode, Li[$Ni_{1-x-y}Ti_xAl_y$]O2, for High-Energy Lithium-Ion Batteries

Geon-Tae Park [a], **Su-Bin Kim** [a], **Been Namkoong** [a], **Nam-Yung Park** [a], **Hun Kim** [a], **Chong S. Yoon** [b,c,*], **Yang-Kook Sun** [a,c,*]

[a] Department of Energy Engineering, Hanyang University, Seoul 04763, South Korea
[b] Department of Materials Science and Engineering, Hanyang University, Seoul 04763, South Korea
[c] Department of Battery Engineering, Hanyang University, Seoul 04763, South Korea

For the sustainable development of Li[$Ni_xCo_yMn_{1-x-y}$]O_2 and Li[$Ni_xCo_yAl_{1-x-y}$]O_2 cathodes, reducing the reliance on cobalt, which is extremely expensive with a fluctuating price and supply uncertainty, is considered essential. In this study, we propose a highly stable Co-free Ni-rich layered cathode developed through a new doping strategy that incorporates heteroelements at different doping stages, including the introduction of Ti during $Ni(OH)_2$ synthesis and doping excess amounts of Al during the lithiation step. The multi-stage engineering strategy guarantees structural durability and electrochemical cycling stability of the inherently unstable LNO to a commercially viable level. Combined with particle surface protection, the Li[$Ni_{0.951}Ti_{0.008}Al_{0.041}$]$O_2$ cathode retains 72.0% of its initial capacity after 3500 cycles, which is unprecedented among previously reported Co-free cathodes. The proposed Co-free cathodes can meet the energy density required for next-generation electric vehicles, as the cathode delivers 890 Wh $kg^{-1}_{cathode}$, and presents a clear breakthrough for the development of commercially viable LNO cathode.

Keywords: Ni-rich layered cathode; New doping strategy; Microstructure engineering; Surface protection; Long-life battery

Introduction

Since the global blueprint for carbon net zero emissions has been drawn, a part of the internal combustion engine (ICE) market share of vehicles has been continually shifting toward electric-powered public and personal transportation. At this rate, electric vehicles (EVs) are expected to greatly transform the future of ground transportation. However, the serious remaining challenges regarding the price and performance issues of lithium-ion batteries (LIBs), which are the primary power source for EVs, have impeded the large-scale adoption of EVs. The average price of a LIB pack, which once exceeded US$4,500 per kWh, has greatly reduced to US$150 per kWh but is still much higher than the contestability target of US$100 per kWh set by the US Department of Energy [1]. The reason for the high cost is the cathode, which largely determines the overall price and performance of a LIB [2,3]. Currently, Co-containing layered Li[Ni_x-Co_y(Al or Mn)$_{1-x-y}$]O_2 (Al = NCA or Mn = NCM) cathodes are deployed as the archetypal cathodes in commercial LIBs [3–5]. Solving the affordability issue of current layered cathodes requires reducing the reliance on Co, which is extremely expensive with supply uncertainty. In fact, the price of Co increased from US$26,000 per ton in 2019 to US$82,000 per ton in 2022, within only three years [6]. The sharply rising demand for LIBs,

---

* Corresponding authors at: Department of Materials Science and Engineering, Hanyang University, Seoul 04763, South Korea; Department of Battery Engineering, Hanyang University, Seoul 04763, South Korea (C.S. Yoon). Department of Energy Engineering, Hanyang University, Seoul 04763, South Korea; Department of Battery Engineering, Hanyang University, Seoul 04763, South Korea (Y-K. Sun).

E-mail addresses: Yoon, C.S. (csyoon@hanyang.ac.kr), Sun, Y.-K. (yksun@hanyang.ac.kr).

https://doi.org/10.1016/j.mattod.2023.11.006

in turn, poses serious supply challenges in terms of the availability of raw materials [7]. Moreover, the elimination of Co from the current family of layered oxide cathode materials has been pushed, as the mining and refining of cobalt ore involve environmental and ethical concerns, including child exploitation [8,9]. Therefore, the development of Co-free cathode material has emerged as important for the sustainable development of high-capacity layered cathodes.

The aim of developing Co-poor or Co-free cathodes has led to an interest in $LiNiO_2$ (LNO) [10–15]. LNO is one of the most promising cost-effective Co-free cathodes for LIBs because the cathode can achieve a high specific capacity of over 250 mAh g^{-1} with a typical upper voltage of 4.3 V versus Li^+/Li [14]. However, its poor cycling durability and thermal instability make its practical use difficult [16,17]. For the practical use of LNO, several issues, including the structural instability at deep state-of-charge (SoC), strain-induced microcracking, vigorous reactivity of highly labile Ni^{4+}, and the ensuing gas evolution problems, must be resolved. Numerous efforts have been devoted to improve the intrinsic instability of LNO cathodes. Composition modification through cation doping (Al, Ga, Mg, Mn, Ti, and W) and anion doping (F, S, and Cl) have been proposed to reinforce the structural durability of the cathode; however, the performance improvement is limited and remain unsatisfactory [11,15,18–24]. Surface coating (Li_2ZrO_3, V_2O_5, and Li_3PO_4) alleviates the inherent cathode-electrolyte interface reactivity of LNO; however, the improvements in cycling stability are marginal as it does not remedy the microcracking issue at high SoC [25–27]. Recently, single-crystalline materials or microstructurally altered LNO cathodes have been reported to resolve the durability issue against intergranular cracking; however, they have yet to achieve long-term cycling stability, which is essential for the deployment of cathode materials in EV batteries [28,29].

In this study, we propose a highly stable Co-free Ni-enriched layered cathode based on LNO through a new doping strategy that incorporates heteroelements at different doping stages, *i.e.*, the introduction of Ti during $Ni(OH)_2$ synthesis and doping excess amounts of Al during the lithiation step. The multi-stage doping strategy offers distinct advantages, enabling sequential microstructure engineering in the wet doping of the precursor and the dry doping during lithiation. Ti was chosen as a dopant for $Ni(OH)_2$ due to its compatibility with wet doping during coprecipitation. Unlike most of the high valent doping elements that do not dissolve into the metal solution or hydroxide solution, $Ti(SO_4)_2$ can be dissolved into the metal solution, enabling the synthesis of Ti-doped $Ni(OH)_2$ precursor. In the case of Al doping, the dry doping method is adopted. The multi-stage engineered cathode remarkably improves the electrochemical performance and thermal stability of LNO, representing a next-generation ternary Co-free layered cathode, $Li[Ni_{0.951}Ti_{0.008}Al_{0.041}]O_2$ (denoted as NTA). The NMA ($Li[Ni_{0.883}Mn_{0.056}Al_{0.061}]O_2$) cathode, previously reported by Li et al., can be regarded as a parallel to the NTA cathode; however, the Ni content in the proposed NTA cathode is 95% which is more challenging to ensure the necessary cycling stability for EVs [30]. In addition, the exceptional multi-stage engineering approach provides means to optimize the cathode microstructure in the NTA cathode. In combination with cathode surface protection, *i.e.*, electrolyte modification or cathode surface coating, the cathode retains 72.0% of its initial capacity after 3,500 cycles, which is the state-of-the-art for Co-free layered cathodes. To determine the underlying mechanism of the dramatic performance improvement of the proposed multi-stage engineered NTA cathode, we investigated a series of LNO and NTA cathodes having a fixed Ti content with different Al contents in terms of crystal structure, morphology, surface properties, structural durability, and extent of gas evolution, and performed its post-mortem analyses after cycling. The Al-doped cathodes, in which the $Ni(OH)_2$ was mixed with Li sources and Al compounds at a molar ratio of Li:Ni:Al = 1.01:1-x:x, are denoted as LNO-Al2 for $x = 0.02$, LNO-Al4 for $x = 0.04$, and LNO-Al6 for $x = 0.06$, respectively. For the Ti- and Al-doped cathodes, in which the Ti 0.75 mol%-doped $Ni(OH)_2$ was mixed with Li sources and Al compounds at a molar ratio of Li:(Ni + Ti):Al = 1.01:1-x:x, the cathodes are denoted as Ti0.75-LNO for $x = 0$, Ti0.75-LNO-Al2 for $x = 0.02$, NTA for $x = 0.04$, and Ti0.75-LNO-Al6 for $x = 0.06$, respectively.

Materials and methods

Synthesis of Co-free NTA cathode materials

$Ni(OH)_2$ (cathode material precursor) was synthesized *via* a co-precipitation reaction in a batch-type reactor (47 L) as described earlier [14]. For the synthesis of the Ti-doped $Ni(OH)_2$ precursor, an aqueous solution of $NiSO_4·6H_2O$ (Samchun Chemicals) and Ti $(SO_4)_2$ (Junsei Chemicals) was prepared in a Ni:Ti molar ratio of 99.25:0.75. Except for the metal composition ratio of the prepared metal sulfate solution, the rest of the synthesis process was the same as that for the $Ni(OH)_2$ precursor synthesis. The $Ni(OH)_2$ and Ti-doped $Ni(OH)_2$ precursors were mixed with $LiOH·H_2O$ (Sigma-Aldrich) and $Al(OH)_3·3H_2O$ (Sigma-Aldrich) at a molar ratio of Li:(Ni + Ti):Al = 1.01:1-x:x; $x = 0$, 0.02, 0.04, and 0.06 for the pristine LNO (without dopants) and Tiy-LNO-Alx cathodes ($y = 0$ for the cathodes without Ti doping and $y = 0.75$ for the Ti-doped cathodes), respectively. The mixed materials were calcined in a tube furnace (Lindberg, Thermo Fisher) for 10 h at 650 °C and 680 °C for the cathodes without and with Ti doping, respectively, under an O_2 atmosphere (heating and cooling rate: 2 °C min^{-1}). Each calcination temperature was optimized based on the electrochemical test results (Fig. S1). For the synthesis of the 1 mol% F-coated NTA cathode, NTA and NH_4F (Sigma-Aldrich) were mixed at a molar ratio of (Ti + Ni + Al):F = 1:0.01 *via* ball-milling for 2 h using a zirconia ball. The mixed powder was heated at 400 °C for 5 h in a tube furnace under an O_2 atmosphere to form an F-coating layer on the surface of the cathode particles.

Analytical approach

The chemical composition of each material was determined using inductively coupled plasma–optical emission spectrometry (ICP-OES; Optima 8300, PerkinElmer). The ICP-OES results of the synthesized cathode materials confirmed their chemical compositions and corroborated their successful syntheses (Table S1). To analyze the cross-sectional morphology of the materials, electrodes were prepared and cut using a cross-sectional polisher (CP; IB-19520CCP, JEOL). The morphologies and cross-sections of the particles were analyzed using scanning electron microscopy (SEM; Verios G4UC, FEI). To quantitatively measure the

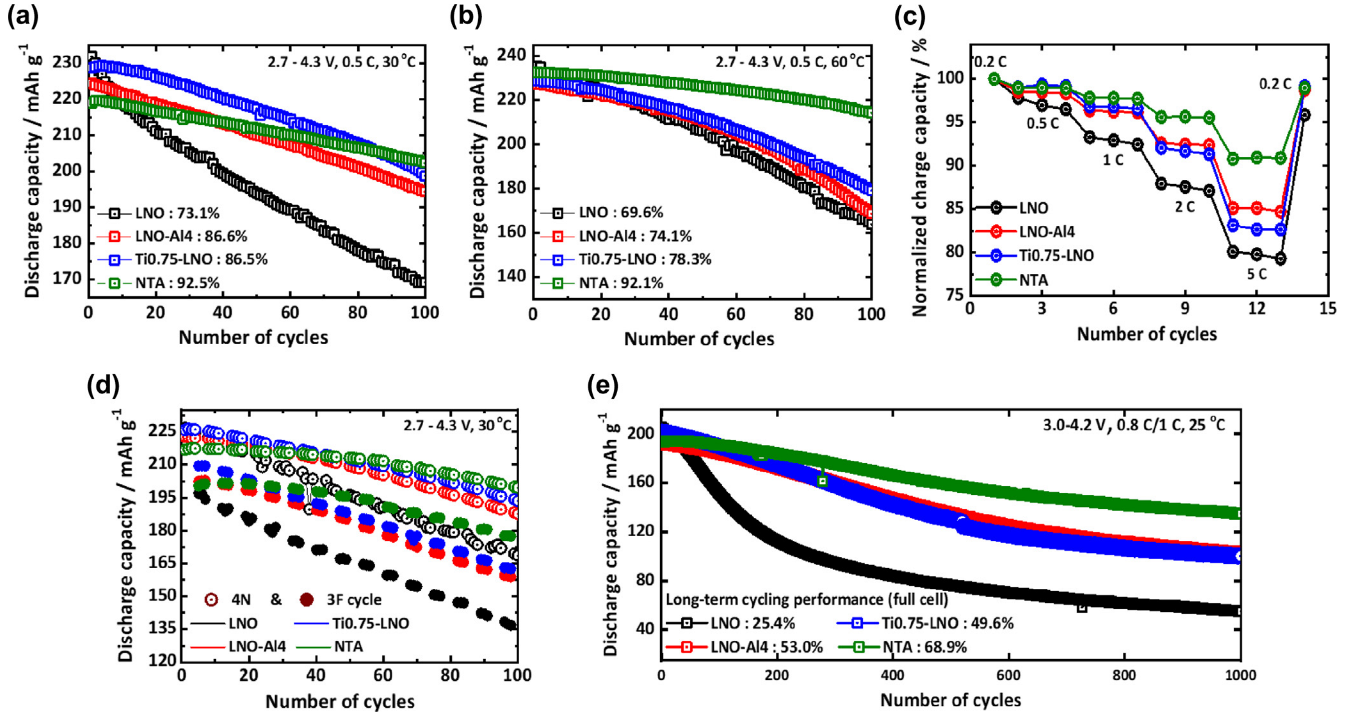

FIG. 1

Comparison of the electrochemical performances of the LNO, LNO-Al4, Ti0.75-LNO, and NTA cathodes: Cycling performances of the half-cells at (a) 30 °C, and (b) 60 °C. (c) Charge rate capabilities of the half-cells. (d) Cycling performances of the half-cells, which are alternately charged at 0.5 C for four cycles (4N) and 3 C for three cycles (3F) at a time (the discharge C-rate is fixed at 0.5 C). (e) Long-term cycling performance of pouch-type full cells using graphite as an anode.

width, length, aspect ratio, and number density of the primary particles and the areal fraction of microcracks, at least three cathode particles from each cathode were selected, and an image processing software (ImageJ) was utilized. The thermal stability of the cathodes was measured using a differential scanning calorimeter (DSC 214 Polyma, Netzsch). For the DSC analysis, a coin-type half-cell was charged to 4.3 V and disassembled in an Ar-filled glove box. The recovered cathode was rinsed and dried with a dimethyl carbonate (DMC) solution, and the electrode was scratched to obtain a powder-type material. The two electrolytes, *i.e.*, 1.2 M $LiPF_6$ in EC:EMC = 3:7 (v/v) + 2 wt% VC (reference electrolyte, Panax Etec) and 1.0 M $LiPF_6$ in EMC:FEC = 3:1 (v/v) + 0.05 M LiDFOB (EF31D), were used to analyze the DSC profile. The charged cathode powder (7 mg) and fresh electrolyte (100 μL) were placed in a high-pressure stainless steel crucible and packed with a gold-plated copper seal. Measurements were carried out by raising the temperature from 30 °C to 350 °C at a rate of 5 °C min^{-1}. The crystal structures of the cathode materials were investigated through X-ray diffraction analysis (XRD; Empyrean, PANalytical) using a diffractometer X-ray detector (PIXcel 1D; PANalytical), equipped with a Cu Kα radiation source. The data were recorded within the 2θ range of 10° and 130° at a step width of 0.02°. The obtained XRD patterns were analyzed using the Rietveld refinement program, FullProf. The sample for TEM analysis was prepared in a Mo lift-out grid by cutting the particles into thin foil using a focused ion beam (FIB, JEM-2100F, JEOL). The crystal structures and elemental distribution of the Al dopant were investigated using transmission electron microscopy combined with a Cs corrector and cold-field emission gun (Cs-corrected TEM; JEM-ARM200F, JEOL, and Talos F200X, FEI). For *in situ* XRD measurements, a pouch-type half-cell was charged at a constant current density of 0.05 C (9 mA g^{-1}) to 4.5 V, measured in transmission mode using an X-ray detector (PIXcel 1D, PANalytical) and recorded every 40 min. For the pouch swelling test, a half-cell was charged to 4.3 V, and the cathode (3 cm × 5 cm) was recovered by disassembling the half-cell. The obtained delithiated cathode was rinsed with DMC and dried. To fabricate a pouch seal, reference electrolyte (Panax Etec) was added in an amount 3.5 times that of the cathode active material and packed in a pouch form. The pouch seal containing the delithiated cathode and electrolyte was stored in a 60 °C oven, and the volume variation was periodically monitored using a hydrometer (MDS-300, Alfa Mirage). Time-of-flight secondary ion mass spectrometry (TOF-SIMS) using a mass spectrometer (TOF-SIMS-5, ION-TOF) equipped with a 30 keV Bi^+ primary ion gun and a 500 eV Cs^+ sputter gun was used to investigate the distribution of elements according to the depth of the electrode in negative mode. X-ray photoelectron spectroscopy (XPS, K-alpha plus Thermo, Thermo Fischer Scientific) was used to investigate the compounds in the cathode-electrolyte interface layers of the cycled cathodes.

Electrochemical tests

The cathode for the electrochemical test was prepared by mixing 90 wt% of the cathode material, 5.5 wt% of the carbon conductive material, and 4.5 wt% of poly(vinylidene fluoride) (PVDF) with an NMP solvent using a mixer (ARE310, Thinky). The mixed slurry was coated on Al foil (UACJ) with an active material loading of 4–5 mg cm^{-2}. The coated electrodes were dried at 110 °C in a vacuum oven, roll-pressed, and punched into disks with diameters of 14 mm. Using Li metal (Honjo Metal) as the anode, micro polypropylene/polyethylene/polypropylene (PP/PE/PP; Celgard 2320, Celgard) as the separator, and a reference electrolyte solution, 2032coin-type half-cells (Hohsen) were fabricated in a glove box filled with Ar. In the galvanostatic test, the cells were cycled at 30 °C at a constant current density of 0.1 C (18 mA g^{-1}) during the first cycle and subsequently cycled at 0.5 C (90 mA g^{-1}) in the voltage range of 2.7–4.3 V (vs. Li$^+$/Li) (Toscat-3100, Toyo). The charge rate capability of the cathode was tested by conducting a galvanostatic test in the voltage ranges of 2.7–4.3 V (vs. Li$^+$/Li) with increasing charge current densities (18 (0.1 C) – 36 (0.2 C) – 90 (0.5 C) – 180 (1 C) – 360 (2 C) – 900 (5 C) – 36 (0.2 C) mA g^{-1}), while the discharge current density was fixed at 0.2 C. For the long-term cycling performance evaluation, a pouch-type full-cell was fabricated. The cathode was prepared by mixing the active material, conductive material, and PVDF at a ratio of 94:3:3 with the NMP solution. The slurry was coated on a carbon-coated aluminum foil with a size of 3 cm × 5 cm and an active material mass loading level of 9–10 mg cm^{-2}. Electrochemical full-cell tests were performed using two electrolytes, the reference and EF31D electrolytes (0.8 mL). A pouch-type full-cell was made of a graphite double-sided coated anode (ENERTECH) and two pairs of cathodes with a capacity balance (N/P) in the range of 1.15–1.2. The cells were cycled at 25 °C with a charge current density of 0.8 C and a discharge current density of 1 C in a voltage range of 3.0–4.2 V. Electrochemical impedance spectroscopy (EIS) was performed in a frequency range of 1.0 mHz–1.0 MHz with a voltage amplitude of 10 mV using a multi-channel potentiostat (VMP3, Bio-Logic) after charging the half-cell to 4.3 V.

Results and discussion

The fundamental electrochemical performances of the synthesized cathodes were characterized in half-cells in the voltage ranges of 2.7–4.3 V. By doping Al and Ti, the intensity of the discharge redox peak near 3.5 V decreases, while the peak position shifts to a higher potential, extracting discharge capacity over a wide range of voltage (Fig. S2). The initial discharge capacity of the cathodes decreased with the increasing fraction of the Al doping amount, owing to their lower fraction of redox-active

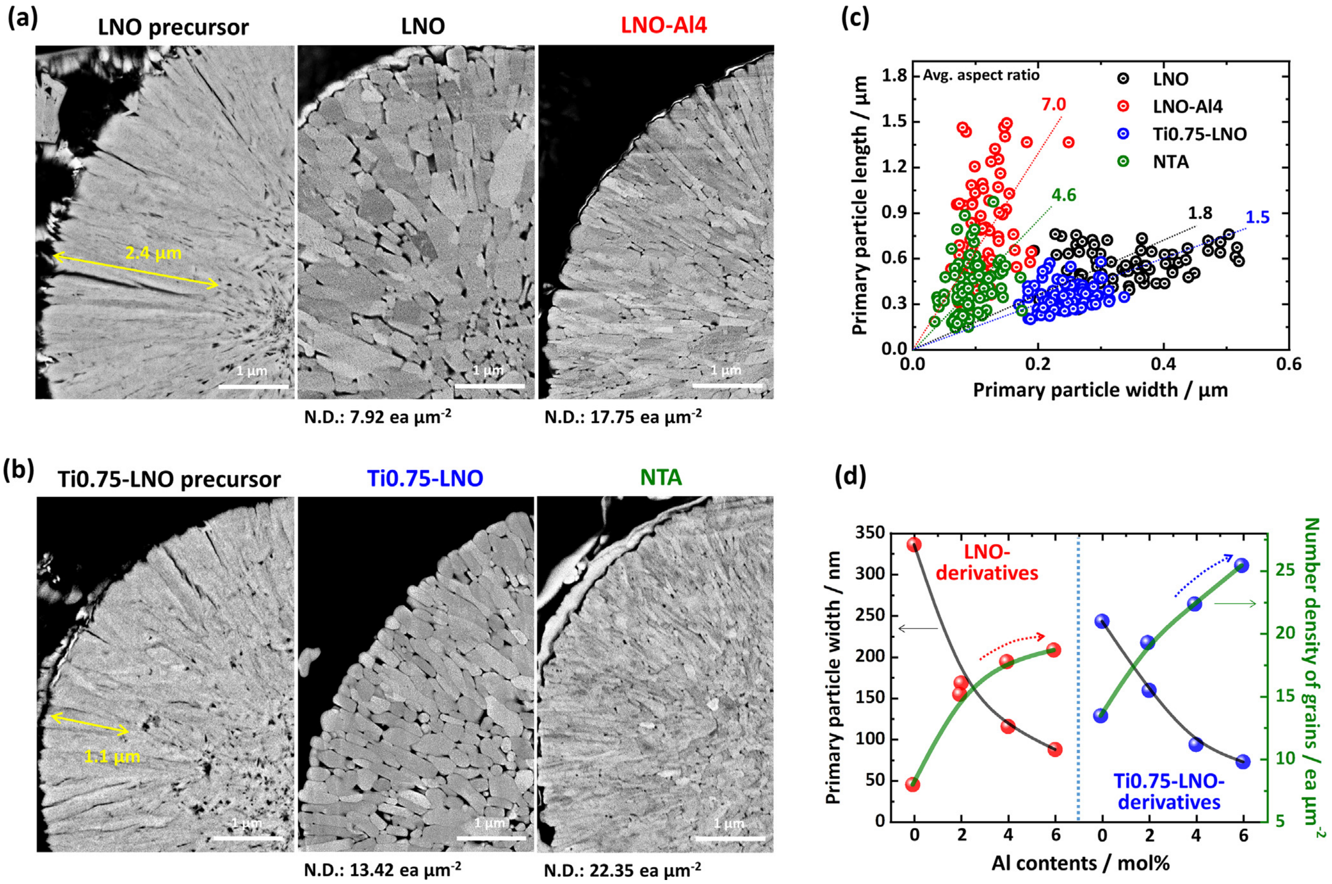

FIG. 2

Cross-sectional SEM images and quantitative morphological characteristics of the cathodes: (a) Cross-sectional SEM images of LNO precursor and its derivative cathodes (LNO and LNO-Al4). (b) Cross-sectional SEM images of Ti0.75-LNO precursor and its derivative cathodes (Ti0.75-LNO and NTA). N.D. represents number density of primary particles within cathode secondary particle. (c) Measured length and width of primary particles in the LNO, LNO-Al4, Ti0.75-LNO, and NTA cathodes. (d) Plot of primary particle width and number density of grains of LNO- and Ti0.75-LNO-derivative cathodes as functions of Al doping contents.

Ni: 250.2 mAh g^{-1} for LNO, 247.3 mAh g^{-1} for Ti0.75-LNO, 242.5 mAh g^{-1} for LNO-Al4, and 240.9 mAh g^{-1} for NTA. However, the cycling stability of the cathodes was markedly enhanced, compensating for the reduced capacity. The Ti wet-doped Ti0.75-LNO cathode retained 86.5% of its initial capacity after 100 cycles, whereas the Al dry-doped cathode, LNO-Al4 exhibited a capacity retention of 86.6% after the same number of cycles (Fig. 1a). The multi-stage engineered NTA cathode exhibited outstanding electrochemical cycling stability, retaining 92.5% of its initial capacity after 100 cycles, which is 19.4% greater than that of the baseline LNO cathode. Moreover, at 60 °C, where the vigorous electrolyte attack accelerates the deterioration of Ni-rich cathodes, the NTA cathode exhibited superior cycling performance, delivering 214.3 mAh g^{-1} after 100 cycles, whereas the LNO, Ti0.75-LNO, and LNO-Al4 cathodes exhibited only 163.8, 179.2, and 168.6 mAh g^{-1}, respectively (Fig. 1b). What makes its cycling stability remarkable is that the cell was operated at 100% depth of discharge (DoD), unlike the currently deployed layered cathode, whose DoD is limited to 60–80% to compensate for capacity fading and guarantee the required battery life. The degradation of LNO cycled above 4.2 V is closely associated with the H2-H3 phase transformation [14]. To monitor the changes in the H2-H3 redox peak, the peak areas of the differential capacity profiles were compared (Fig. S3). The redox peak (H2-H3) area of the cell featuring the LNO cathode quickly decreased to 34.4% of the initial peak area after 100 cycles. However, the LNO-Al4, Ti0.75-LNO, and NTA cathodes retained 75.8, 59.1, and 90.8%, respectively, of their initial peak areas after 100 cycles, substantiating the outstanding phase transition reversibility of the NTA cathode. Fast charging capability, one of the key requirements for EV operation, was tested by increasing the charge current density to 5 C. The results show that the NTA cathode delivered 90.9% of the 0.2 C capacity at 5 C, whereas the baseline LNO cathode delivered only 79.7% (Fig. 1c). The origin of the improvement in fast charging for NTA cathode is discussed later. To better demonstrate the outstanding rate capability and cycling stability of NTA, the cathodes were tested using a 4N-3F cycle protocol which simulates the real operating conditions of LIBs in EVs; *i.e.*, alternately charging the half-cells at 0.5 C for four cycles and at 3 C (fast charge) for three cycles at a time (Fig. 1d). Through repeated cycling under harsh operating conditions, NTA retained 88.5% of its initial capacity after 100 cycles at 3 C. In contrast, LNO, LNO-Al4, and Ti0.75-LNO retained 69.8, 78.5, and 77.6%, respectively. The outstanding cycling stability of the NTA cathode was further demonstrated by its long-term cycling performance in pouch-type full cells (Fig. 1e). While LNO lost more than 50% of its initial capacity after only 300 cycles, NTA retained 68.9% of its initial capacity even after 1000 cycles.

To understand the microstructural evolution of the Co-free NTA cathode achieved by sequential Ti wet doping and Al dry doping, the morphology of the unmodified LNO hydroxide precursor and the subsequent lithiated oxide were investigated first. Fig. 2a and Fig. S4 show that the $Ni(OH)_2$ precursor reveals a highly oriented geometry in which ~2.4 μm-long rod-like primary particles are aligned in the radial direction of a spherical secondary particle. High-temperature calcination of the hydroxide precursor induced extensive coarsening of needle-like primary particle bundles and produced thick, bulky, and near-equiaxed-shaped primary particles, eliminating the initial precursor morphology [31,32]. However, when 4 mol% Al was added during the lithiation of the hydroxide precursor, the consolidation of the primary particles was effectively prevented, preserving the rod-like precursor morphology in the lithiated cathode. When the Al doping level is 1 – 2 mol%, Al doping has no visible effect on the cathode microstructure; however, when the Al composition exceeds the solubility limit, Al ions segregate at the interparticle boundaries and alter the primary particle morphology by retarding coarsening. The TEM-EDX elemental line scan revealed that the Al dopants segregated at the interparticle boundaries retarded the consolidation of primary particles and helped to maintain the radially aligned rod-like precursor morphology despite the high-temperature calcination (Fig. S5). The primary particles progressively elongated and became radially oriented with increasing fractions of Al (Fig. S6). The peripheral needle-like primary particles emanating from the particle center of Ti-doped $Ni(OH)_2$ were 1.1 μm in length, which is slightly shorter than that of $Ni(OH)_2$ (Fig. 2b). We believe that the precipitation of titanium hydroxide may partially hinder the continuous growth of $Ni(OH)_2$ primary particles. More voids were observed on the interior of the Ti-doped $Ni(OH)_2$ particle than that of $Ni(OH)_2$; however, the tap density was 2.0 g cc^{-1} for both precursors, indicating that the particle densities were not significantly different. The calcination of the Ti-doped $Ni(OH)_2$ precursor produced grains that were similar in shape but different in size from those of LNO grains. The average aspect ratio, width, and length of primary particles were 1.8, 336 nm, and 564 nm for LNO and 1.5, 243 nm, and 353 nm for Ti0.75-LNO (Fig. 2c). Unlike the cathode with an excess amount of Al dry doping, which retards the coarsening of adjacent hydroxide primary particles to produce rod-like particle morphology, the Ti wet doping process appears to reduce grain size without changing the primary particle shape. Contrary to the wet doping, the Ti dry doping of LNO, *i.e.*, adding Ti during the cathode calcination process, produced elongated primary particles similar to those of the Al dry-doped cathodes (Fig. S7). The results indicate that the choice of doping stage, whether dry or wet, undoubtedly affects morphology evolution. The distinctive feature of Ti wet doping in exclusively engineering the primary particle size without changing the shape is noteworthy. By combining each method, a multi-stage engineered NTA cathode produced nano-sized, rod-like primary particles that were radially oriented and tightly packed. They were extremely small and tightly compacted; thus, the particle number per unit area was the highest for NTA: 22.4 ea μm^{-2} for NTA, 17.8 ea μm^{-2} for LNO-Al4, 13.4 ea μm^{-2} for Ti0.75-LNO, and 7.9 ea μm^{-2} for LNO. Though the primary particle refinement resulted in increment of specific surface area of the cathode material which causes the risk of surface damage (Fig. S8), the outstanding cycling stability of NTA cathode shown in Fig. 1 suggests that ensuring its structural stability surmounts the chemical reactivity issue in improving cycling performance. Obtaining a nanostructured cathode with a high particle number density is not trivial. For example, increasing the Al doping amount to more than 4 mol% can further increase the particle number density of LNO by reducing the widths of the primary particles; however, an oversupply of Al

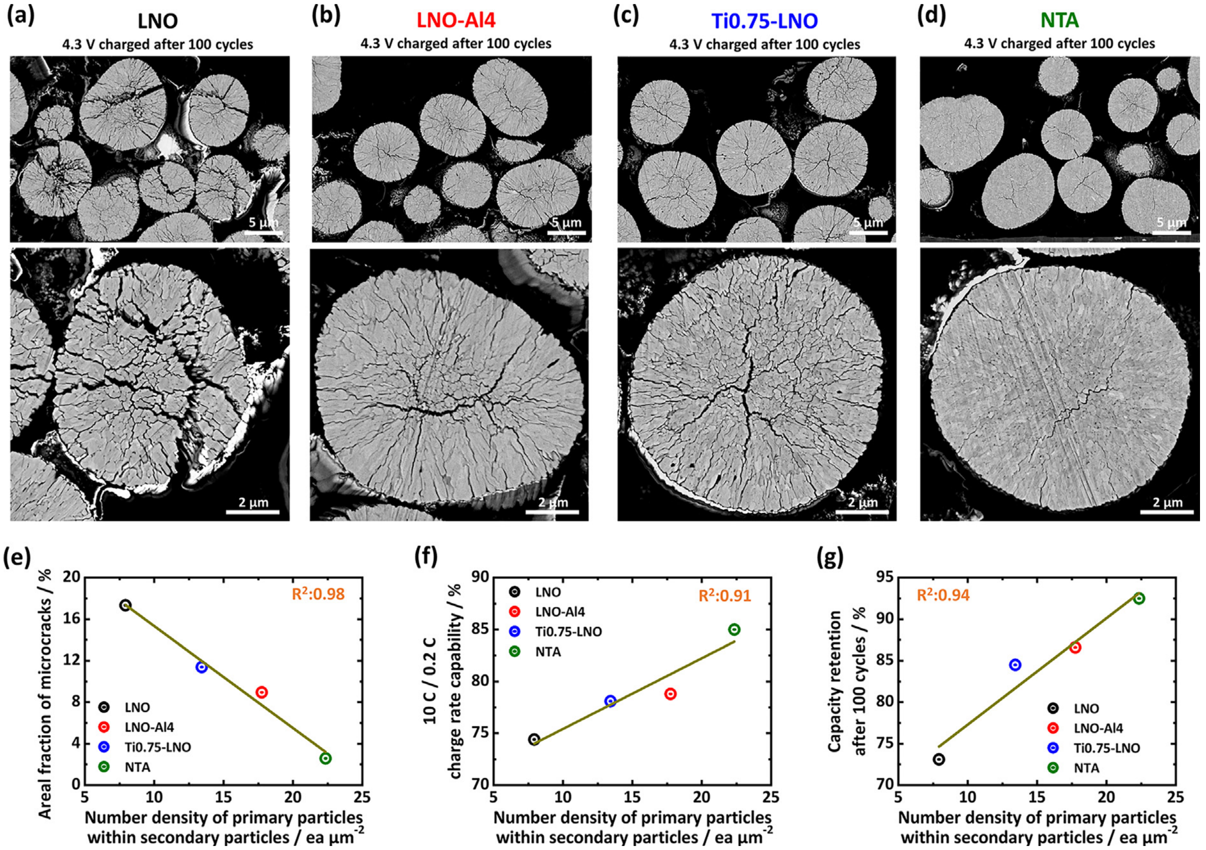

FIG. 3

Microstructural durability of the cathodes and its correlation with number-density of primary particles and electrochemical performances: Cross-sectional SEM images of the (a) LNO, (b) LNO-Al4, (c) Ti0.75-LNO, and (d) NTA cathodes charged to 4.3 V after 100th cycles. Linear regression plot between number-density of primary particles and (e) areal fraction of microcracks after 100 cycles, (f) 10 C/0.2 C charge rate capability of the cathodes, and (g) capacity retention after 100 cycles.

may inhibit the sintering process that deteriorates the cathode microstructure (Fig. 2d and Fig. S5). Moreover, adding an excess amount of inactive doping elements may hamper (de)lithiation kinetics, leading to a decrease in specific capacity (Fig. S9). In addition, the usual methods of synthesizing ultrafine or nanoceramic materials are implemented under non-equilibrium conditions, requiring specialized methods such as spark plasma sintering, which are not practical for preparing cathode powders [33]. Thus, the multi-stage engineering strategy proved to be effective in constructing spatially aligned nanosized primary particles with an exceptionally high number density.

The extent of the structural degradation of the cathode particles correlates well with their electrochemical cycling stability, as revealed by cross-sectional SEM images of the cathodes recovered after 100 cycles in half-cells. The unmodified LNO particles developed thick and widespread intergranular microcracks after cycling. Most of the secondary particles were pulverized into several fragments, and the constituent primary particles disintegrated into individual grains (Fig. 3a). In addition, the long and thick microcracks extended to the cathode particle surfaces, providing channels for the liquid electrolyte to penetrate the cathode particle interior. The increase in the cathode-electrolyte contact area resulted in a vigorous parasitic reaction throughout the cathode particles and irreversibly damaged the cathode by forming electronically insulating NiO-like impurity layers [17,34–39]. In the case of the LNO-Al4 cathode, the formation of rod-like, elongated primary particles largely suppressed the formation of microcracks, improving the electrochemical cycling performance (Fig. 3b). However, the thin microcrack networks propagated along the interparticle boundaries, exposing the particle interior to the electrolyte. As a result, the improvement in cycling stability was limited, especially under harsh electrochemical cycling conditions (60 °C), where the cathode-electrolyte reactivity intensifies (Fig. 1b). Decreasing the grain size of the LNO cathode by Ti wet doping alleviated the accumulation of internal strain; however, the micro-fractures that traversed the entire secondary particle, which eventually compromise the structural integrity, persisted (Fig. 3c). The most effective method for mitigating microcrack formation is a multi-stage engineering strategy. The NTA cathode, comprising radially oriented nanosized primary particles with a high particle number density, remained mechanically intact without visible intergranular microcracks after the same number of cycles (Fig. 3d). Hairline cracks were visible only in the magnified cross-sectional SEM image and were almost arrested before reaching the surface, protecting the particle interior from direct contact with the electrolyte. The observed mechanical stability of the NTA cathode correlates well with its superior electrochemical cycling perfor-

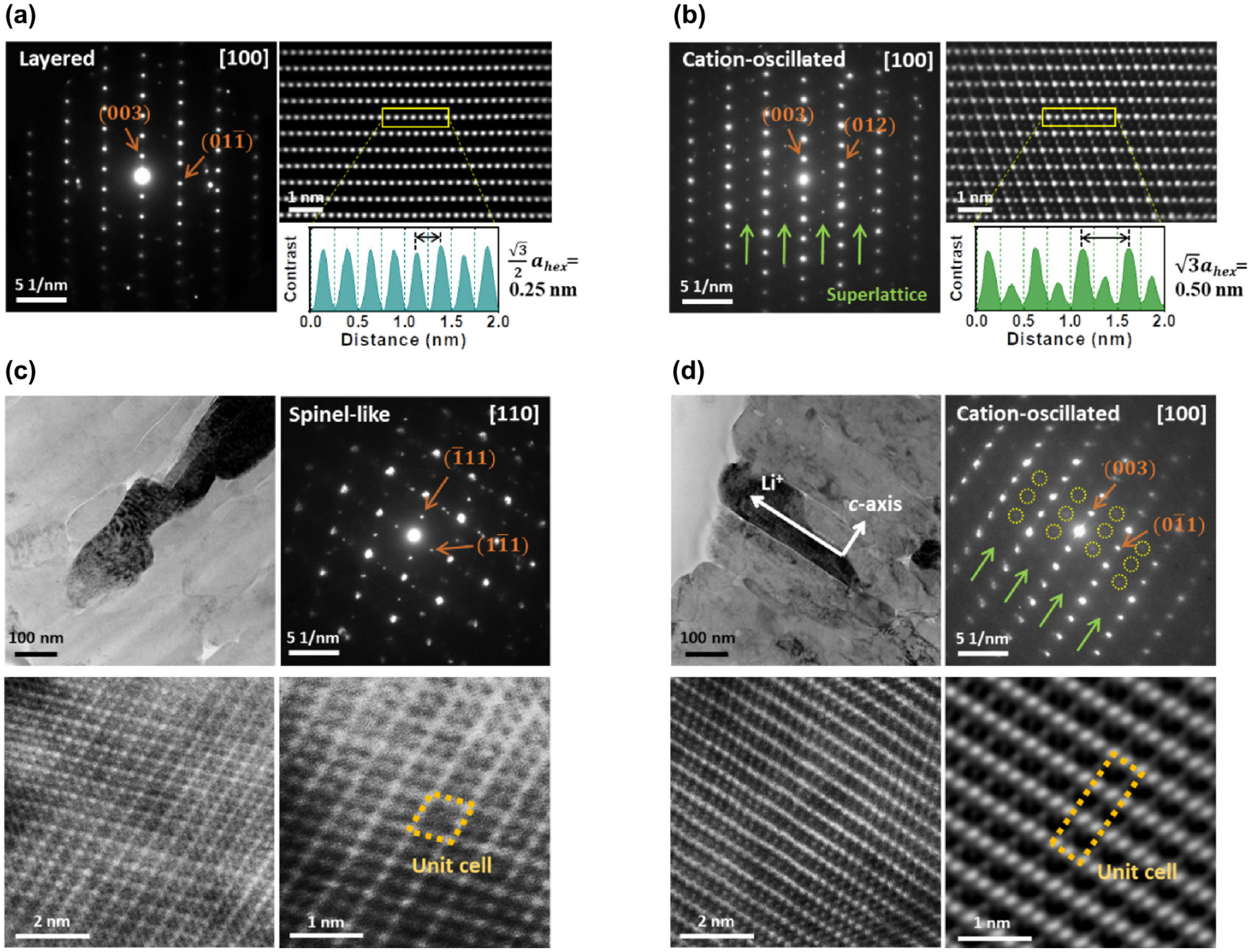

FIG. 4

Comparison of structural stability of LNO and NTA cathodes: SAED, high-angle annular dark-field (HAADF) TEM images, and contrast line scans of the TM layer of the (a) LNO and (b) NTA cathodes. Bright-field TEM images, SAED, and corresponding HR-TEM images of delithiated (c) LNO and (d) NTA cathode particles, *i.e.*, charged to 4.5 V.

mance, with 92.1% of its initial capacity being retained after 100 cycles, even under harsh operating conditions (60 °C) (Fig. 1b). The benefit of the mitigating the crack formation is further demonstrated by differential scanning calorimetry (DSC) analysis, which shows that the thermal instability of the delithiated NTA cathode was much improved as the cathode-electrolyte contact area is minimized in its charged state (Fig. S10). Interestingly, a correlation exists between the number density of primary particles and several performance indicators. The degree of microcracking was estimated by measuring the areal fraction of the cracks using image analysis software and plotted against the number density of the primary particles, as shown in Fig. 3e. The plot reveals an approximate linear relationship, demonstrating the effectiveness of the particle size refinement in suppressing microcracks. Nano-size primary particles increase the fraction of particle boundaries per area which deflect crack propagation and dissipate the strain energy [40–42]. The rate capability also linearly scales the number density as the numerous interparticle boundaries provide short-circuit diffusion paths (Fig. 3f). Li^+ migration through relatively loose atomic arrangements at interparticle boundaries is much faster than through the bulk as observed in the deterioration of the rate capability of single-crystalline layered cathodes [35,43,44]. The beneficial effects of the particle size refinement helped to improve the cycling stability as the cycling also exhibits an approximate linear relationship with the particle number density (Fig. 3g). Fig. 3-e-3g demonstrate that the particle size and shape engineering can sufficiently guarantee the electrochemical performance of Ni-rich layered cathodes despite the absence of cobalt and manganese in their compositions.

As is generally known, the presence of Co^{3+} and Mn^{4+} cations in the cathode host structure provides the cathode with significant structural stability. Co^{3+} with S (spin state) = 0 lowers Li^+/Ni^{2+} cation mixing by alleviating the magnetic frustration among the transition metal cations [45]. In addition, the presence of Co^{3+} inhibits the cooperative Jahn-Teller effect in the NiO_2 slab, which suppresses the formation of unwanted monoclinic phases [46]. As for Mn^{4+}, inactive Mn ions stabilize the

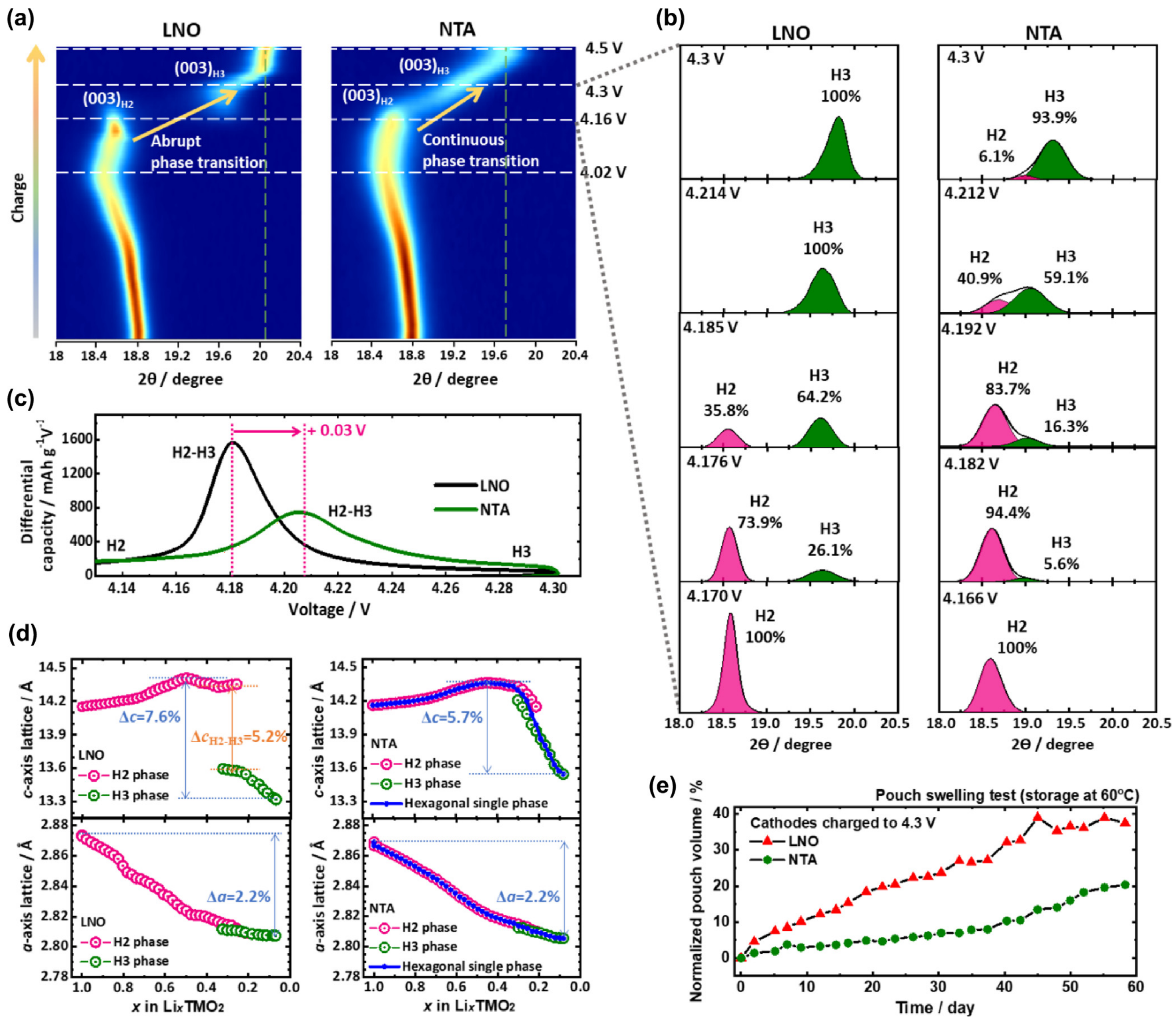

FIG. 5

Phase transition behavior during the charging of the cathodes to 4.5 V investigated via *in situ* XRD measurements and pouch swelling test results of the LNO and NTA cathodes: (a) contour plots of (003) reflection and (b) deconvoluted (003) peaks of the LNO and NTA cathodes during charging the cathodes to 4.5 V. (c) Differential capacity profiles of the LNO and NTA cathodes. (d) Comparison of the *c*- and *a*-axis lattice parameter changes in LNO and NTA cathodes during the *in situ* XRD measurement. (e) Normalized volume variation plots of the pouches containing LNO and NTA cathodes as functions of the number of storage days (60 °C).

structural framework of Ni-rich cathodes by mitigating the abrupt anisotropic lattice contraction and expansion during charge and discharge [47,48]. Accordingly, the Co– and Mn-free LNO cathode pose serious inherent structural instability, particularly in their deeply charged state. For an in-depth investigation of the structural stability of Co-free LNO and NTA cathodes, high-resolution transmission electron microscopy (HR-TEM) was performed before and after charging them to 4.5 V. In the unmodified LNO cathode, the layered phase (space group: $R\bar{3}m$) was verified using XRD and scanning TEM (STEM) (Fig. S11, Table S2, and Fig. 4a). A selected area electron diffraction (SAED) pattern recorded along the [100] zone axis reveals that the LNO cathode is free of streaks and impurities because its diffraction spots are round and sharply defined. The projection of the layered structure in the same direction shows a row of Ni atoms with a periodicity of 0.25 nm in the TM layer and no extra row of Ni atoms in the Li layer, which corresponds to a typical layered structure [32]. However, the [100] zone-axis diffraction pattern of the NTA cathode displayed distinctive rows of extra peaks with relatively weak intensity at $\frac{1}{2}$ spacing along the *c*-axis (Fig. 4b). The extra spots indicate the presence of a superlattice structure in the *a-b* plane. The projection of this superlattice structure along the [100] zone axis shows a row of atoms with a periodicity of 0.5 nm, owing to the partial absence of TM ions in the TM layer. TM sites are alternately occupied by Li^+ ions on every other row and vice versa in the Li layer, creating

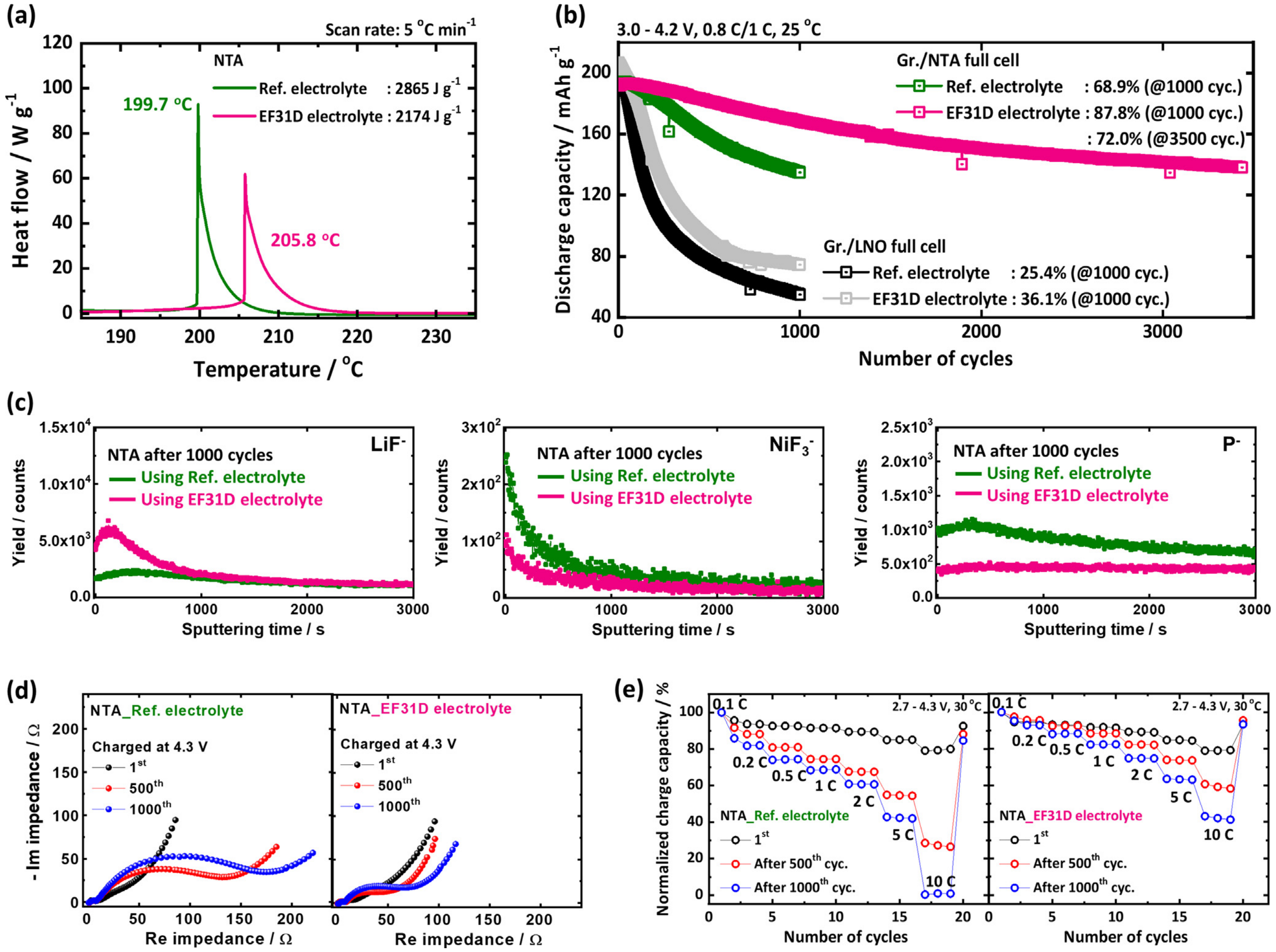

FIG. 6

(a) DSC profiles of NTA cathode in their charged state in the presence of the reference and EF31D electrolytes, respectively. (b) Long-term cycling performances of pouch-type full cells featuring graphite (Gr.) anodes and LNO and NTA cathodes in the presence of the reference or EF31D electrolyte. (c) ToF-SIMS depth profiling of the ion species in the cathode-electrolyte interfaces (CEI) of the cycled NTA cathodes using the reference and EF31D electrolytes, respectively. Variations of (d) Nyquist plots obtained from EIS results and (e) charge rate capabilities of NTA cathodes after 1st, 500th, 1000th cycles using the reference and EF31D electrolytes, respectively.

a superstructure unit cell. Such intermixing of TM and Li^+ ions in an ordered manner is different from the typical random intermixing of Li^+ and TM ions, *i.e.*, cation mixing, reported in the literatures. We denote the ordered TM and Li^+ intermixed structure as a cation-oscillated structure. The structure is similar to the previously observed cation-ordered structures in $Li[Ni_{0.5}Mn_{0.5}]O_2$, which produced superlattice diffraction spots through the ordering of the cations in the TM layer [49]. As the formation of Ni^{2+} and its migration into the Li slab are prerequisites for the oscillating intermixing of Li^+ and Ni^{2+}, partial substitution of Ni^{3+} ions with dopants whose oxidation state is higher than 3+, *e.g.*, Ti^{4+} promotes the evolution of cation-oscillated structures, as demonstrated in Zr-0.4 mol%-doped LNO [13]. The superlattice diffraction spots observed in Ti0.75-LNO cathode further substantiate the hypothesis (Fig. S12). To compare the stability of the cathodes in their delithiated structures, LNO and NTA were charged to a voltage of 4.5 V (vs. Li^+/Li), at which nearly 93% of the Li^+ in the host structure was removed. The SAED pattern recorded along the [1 1 0] zone axis revealed that the delithiated LNO structure transformed into a spinel-like phase, which was characterized by its mirror symmetry (Fig. 4c). A spinel-like structure was also observed for other primary particles in the charged LNO cathode (Fig. S13). The high-resolution TEM image clearly shows the atomic arrangement and unit cells of the spinel-like crystal structure. Such a structural deformation in the deeply charged state likely originated from the lattice collapse and the subsequent oxygen loss [50,51]. The intermittent absence of Li^+ from the host structure results in localized collapse of the layer planes and produces a mixture of $Ni^{3+/4+}$ cations and O^{2-} anion intermediates. By consuming O^{2-} anions, the reactive oxygen intermediates produce CO_2 and CO gases, which leads to a change in the structural framework from layered ($R\bar{3}m$) to spinel ($Fd3m$)-like [50,51]. However, the periodical occupation of TM ions in the Li slab of the NTA cathode, *i.e.*, the cation-oscillated structure preserved its original structural framework even at 4.5 V (Fig. 4d). Primary particles converted to the spinel-like phase were not observed in the charged NTA cathode

(Fig. S14). During the deintercalation of Li^+ ions from the host structure, the TM ions in the Li layer may act as pillars and stabilize the delithiated structure [52,53]. Maintaining a cation-oscillated structure of the NTA cathode at a high SoC is believed to be responsible for the preservation of the Li intercalation reversibility and, accordingly, the enhancement of electrochemical cycling stability.

To systematically monitor the structural transition in detail, *in situ* XRD analysis was performed while charging the cathodes to 4.5 V. As shown in Fig. 5a, the contour plots of the (003) reflections of the LNO and NTA cathodes are nearly identical up to 4.16 V. A marked difference was observed starting at 4.16 V near the onset of the H2-H3 phase transition. The (003) peak of LNO abruptly disappeared after 18.7° and suddenly appeared at an angle nearly 0.9° higher than that of the H2 phase. In contrast, the (003) reflection of the NTA cathode continuously shifted from the H2 phase to the H3 phase without any significant decrease in the peak intensity. Moreover, the extent of the (003) peak displacement in NTA was less than that of LNO; the (003) peak of LNO shifted to 20.1°, whereas the (003) peak of NTA shifted to 19.7°. This result substantiates the structural stability of the cation-oscillated structure by protracting the abrupt shrinkage of the NiO_2 interlayer distance. To quantitatively compare the phase transition behavior, the (003) reflections were deconvoluted and plotted against SoC, as shown in Fig. 5b. For the LNO cathode, two clearly separated symmetric peaks were observed above 4.18 V. Two deconvoluted peaks were observed at approximately 1.1° apart. This complete discontinuity in the phase transition likely induces an abrupt lattice mismatch, which results in the accumulation of a large strain between the two different crystalline domains [11]. In contrast, the NTA cathode revealed the coexistence of two hexagonal phases in a single asymmetric (003) peak. The (003) reflection at 4.17 V broadened asymmetrically toward a higher angle, and the intensity of $(003)_{H2}$ smoothly decreased while that of $(003)_{H3}$ simultaneously increased, which indicates that the abrupt structural distortion had been protracted. Interestingly, the residual H2 phase was still visible in the NTA cathode at 4.3 V. The delay in the H2-H3 phase transition can also be observed from the differential capacity curves in Fig. 5c. The width of the H2-H3 phase transition peak of the LNO cathode was narrow, whereas that of the NTA peak was broad. In addition, the redox peak of NTA shifted toward a higher potential, indicating a delay in the onset of the deleterious H2-H3 phase transition and partial retention of the H2 phase at 4.3 V. Such a delay in the phase transition of NTA suggests that its unique crystal structure effectively protracts the abrupt structural distortion over a wide range of voltages, thereby suppressing the formation of microcracks [11,47]. Based on the phase deconvolution results and the dQ-dV^{-1} curves, the *a*- and *c*-lattice parameters of the cathodes were calculated using a two-phase mixture model. As shown in Fig. 5d, the extent of *c*-axis lattice shrinkage during the H2-H3 phase transition was reduced in NTA by 5.7%, whereas that of LNO contracted by 7.6%. The mismatch of the *c*-axis lattice parameter during the H2-H3 transition ($\Delta c_{\text{H2-H3}}$) was more than half the magnitude of the maximum *c*-axis contraction ($\Delta c_{\max}$) in LNO; $\Delta c_{\text{H2-H3}}$ was 5.2%, while $\Delta c_{\max}$ was 7.6%. The extent of the lattice mismatch was nearly 0.8 Å for LNO, while that of the NTA was only 0.2 Å. As for the *a*-axis lattice parameter, the degree of lattice mismatch was limited to 0.003 Å for both cathodes, rendering the lattice mismatch highly anisotropic. Thus, the anisotropy, which aggravates the structural degradation, was mitigated by atomic structural modification, thus stabilizing the delithiated structures. The structural stability of the NTA cathode was also demonstrated by the pouch swelling test, in which the charged cathode and electrolyte were stored in a sealed pouch at 60 °C for several days to monitor their volume variation. As shown in Fig. 5e, the pouch containing the electrolyte-immersed, delithiated LNO cathode underwent a rapid volume expansion; nearly 40% volume increase was observed after 60 days of storage. However, the volume of the sealed pouch containing the delithiated NTA cathode expanded to only half that containing the LNO cathode after the same period. Additional storage-swelling test results to supplement the reproducibility of the gas evolution experiment are provided in Fig. S15. Such gas evolution mostly originates from the electrolyte decomposition at the cathode-electrolyte interface, which exacerbates when in contact with a structurally unstable Ni-rich layered cathode, such as LNO, as it provides a large contact area with highly reactive Ni^{4+} and intermediate O^{2-} anions throughout the intergranular microcracks [14,17]. Thus, the suppression of gas evolution in the delithiated NTA cathode corroborates its outstanding structural stability despite being challenged at its most vulnerable state at 4.3 V.

Although the structural reliability of the cathode has been considerably reinforced by engineering its microstructure and crystal structure, its long-term cycling performance, which maintains 68.9% of its initial capacity after 1000 cycles, is still insufficient for application in EV batteries requiring long cycle life (Fig. 1e). We suppose that the observed capacity decay originates primarily from the inherent surface chemical instability of the cathode, as labile tetravalent Ni^{4+} ions are prevalent in Ni-enriched cathodes at high SoCs. To alleviate the surface chemical susceptibility-induced performance deterioration, fluoroethylene carbonate (FEC) and lithium difluoro(oxalate)borate (LiDFOB) were introduced into the conventional carbonate-based electrolyte; the composition of the modified electrolyte is 1.0 M $LiPF_6$ in EMC:FEC = 3:1 (v/v) + 0.05 M LiDFOB (denoted as EF31D). The effectiveness of fluorinated electrolytes in cathode materials has been demonstrated in previous studies, as the performance improvement of the cathode is mainly attributed to the formation of a chemically protective lithium fluoride (LiF) layer on the cathode surface [54,55]. The differential scanning calorimetry (DSC) result shown in Fig. 6a verify the chemical stability of EF31D in contact with a highly delithiated Ni-rich cathode. The charged NTA cathode immersed in the EF31D electrolyte produced an exothermic peak at 6.1 °C higher than that of the reference electrolyte (1.2 M $LiPF_6$ in EC:EMC = 3:7 (v/v) + 2 wt% VC) with reduced heat generation, approximately 75% of that of the reference electrolyte. Full cell testing showed that the use of the EF31D electrolyte substantially enhanced the long-term cycling performance of the NTA cathode (Fig. 6b). The full cell featuring NTA cathode and EF31D electrolyte retained 87.8% of their initial capacity after 1000 cycles whereas the full cell using the reference electrolyte delivered a capacity retention of 68.9% after 1000 cycles. The full cell featuring NTA cathode and EF31D electrolyte continued to operate up to 3500 cycles, retaining 72.0% of its initial capacity, which corresponds to 1800 cycles at a capacity retention of 80%. A marked improvement in cycling stability of NTA cathode using EF31D electrolyte may attributable to both the F-coating and Al residues, as the F and Al elements are highly concentrated at the cathode surface shielding the cathode active material from the direct contact with the electrolyte [56]. Such long-term cycling performance over 3500 cycles is unprecedented for Co-free LNO-based cathodes, according to the previous literatures (Fig. S16 and Table S3), whose cycle numbers are limited to within 1000 cycles. As expected from its outstanding structural durability, microcracking-induced damage was not observed in the either cycled cathode, regardless of the electrolyte used (Fig. S17). In contrast, marked differences were identified in the ToF-SIMS and XPS analyses. ToF-SIMS depth profiling of the cathode-electrolyte interface (CEI) layer shown in Fig. 6c indicates the presence of a LiF-rich layer on the surface of the cathode particles cycled in the EF31D electrolyte. In addition, the peak spectra reveal that NiF_3^- secondary ion fragments and P^- species, which represent the degree of TM dissolution and $LiPF_6$ salt decomposition, respectively, are clearly reduced by adopting EF31D. From the XPS analysis, the intensities corresponding to the C=O and O-C-O spectral peaks were lower in the EF31D electrolyte than in the reference electrolyte, whereas the spectra corresponding to LiF were detected at a higher intensity in the cathode using the EF31D electrolyte (Fig. S18). This reinforces our belief that the EF31D electrolyte is less decomposed on the cathode surface during cycling but promotes the formation of a stable LiF compound. As LiF is well-known to resist electrolyte attack, its presence on the cathode surface mitigates surface degradation, thus improving the cycling retention of the cathode. Notably, even though the EF31D electrolyte was adopted, the capacity retention of LNO deteriorated rapidly (Fig. 6b), which substantiates the importance of prioritizing the structural durability of the LNO cathode before ensuring its chemical stability. To investigate changes in electrochemical properties after long-term cycling of the cathodes depending on which electrolyte is used, the cycled cathodes were reassembled into coin-type half-cells with fresh Li metal and electrolytes. The Nyquist plots obtained from the EIS results reveal that the increase in charge transfer resistance (R_{ct}) during cycling was greatly reduced in the EF31D electrolyte compared to the reference electrolyte, demonstrating that thinner decomposition products were deposited on the cathode surface (Fig. 6d and Table S4). The thick impurity layers identified in the cycled cathode in the reference electrolyte hindered the diffusion of Li^+ ions, resulting in an increase in polarization and a loss of rate performance after long-term cycling (Fig. 6e). However, the rate capability of NTA cycled in EF31D was relatively well maintained after the same cycling period. We hypothesize that the performance improvement observed in the EF31D electrolyte is primarily attributable to the LiF coating of the cathode and not solely due to the use of a special electrolyte composition. An additional experiment was conducted to test this hypothesis. An F 1 mol%-coated NTA cathode, that is, a LiF compound coated on the cathode surface in advance, was prepared, and a pouch-type full cell was fabricated with a reference electrolyte (Fig. S19). Given that the full cell featuring the F 1 mol%-coated cathode and reference electrolyte exhibits long-term cycling behavior similar to that of the full cell featuring NTA and EF31D electrolyte, the hypothesis that the performance improvement in the EF31D full cell mainly originates from the LiF surface coating is highly likely. The associated XPS, ToF-SIMS, and EIS results of the F 1 mol%-coated NTA cathode further prove this hypothesis (Fig. S20 and Table S4). In addition, since the cycling stability of the NTA cathode is substantially improved by the EF31D electrolyte or F coating, the extra cost of the electrolyte and coating process easily offsets the battery life gained by the modified electrolyte or F coating. Consequently, the proposed strategy to improve the durability of the highly unstable LNO cathode, *i.e.,* microstructural engineering followed by the protection of chemically unstable cathode surfaces, is demonstrated to guarantee the long-term cycling stability of Co-free Ni-rich layered cathodes. Thus, NTA represents a long-life high-energy–density Co-free cathode, suitable for EVs.

Conclusion

The NTA cathode is proposed as a next-generation, high-energy–density, Co-free cathode for EVs. Multi-stage engineering of the cathode, namely, the introduction of Ti during $Ni(OH)_2$ synthesis followed by an excess amount of Al doping during the calcination step, was demonstrated to produce a novel cathode microstructure in which nano-sized rod-like primary particles are packed with an exceptionally high particle number density. The primary particle size refinement in the LNO cathode remarkably reinforces its structural durability, thereby improving the cycling performance and thermal stability of the cathode. The cation-oscillated structure observed in the NTA cathode mitigated the abrupt anisotropic lattice contraction-induced structural breakdown and alleviated the subsequent oxygen loss problem of the LNO cathode. By securing the surface chemical stability of the cathode by using the EF31D electrolyte, the long-term cycling performance of the NTA cathode was remarkably enhanced, delivering a capacity retention of 72.0% after 3500 cycles in a full cell, which is unprecedented among previously reported Co-free LNO-based cathodes. Considering that the long-term cycling performance of the unmodified LNO cathode decreased rapidly even the EF31D electrolyte was used, ensuring the structural durability of the Ni-rich cathode must be considered a higher priority than securing the chemical stability of the LNO cathode. Thus, the proposed NTA cathode is a highly engineered Co-free layered cathode that can meet the energy density required for next-generation EVs and represents a breakthrough in the sustainable development of commercially viable LNO cathodes.

CRediT authorship contribution statement

Geon-Tae Park: Conceptualization, Investigation, Methodology, Visualization, Writing – original draft. **Su-Bin Kim:** Investigation, Validation. **Been Namkoong:** Investigation, Validation. **Nam-Yung Park:** Investigation, Methodology. **Hun Kim:** Investigation, Validation. **Chong S. Yoon:** Investigation, Methodology, Writing – review & editing. **Yang-Kook**

Sun: Conceptualization, Supervision, Writing – review & editing, Funding acquisition, Project administration.

Data availability

The raw/processed data required to reproduce these findings cannot be shared at this time due to legal reasons.

Declaration of Competing Interest

The authors declare that they have no known competing financial interests or personal relationships that could have appeared to influence the work reported in this paper.

Acknowledgements

This work was supported by the Human Resources Development Program (No. 20214000000320) of the Korea Institute of Energy Technology Evaluation and Planning (KETEP), funded by the Ministry of Trade, Industry, and Energy of the Korean government.

Appendix A. Supplementary data

Supplementary data to this article can be found online at https://doi.org/10.1016/j.mattod.2023.11.006.

References

[1] US Department of Energy (2020), 2020 Annual Merit Review, Vehicle Technologies, https://www.energy.gov/sites/prod/files/2020/06/f75/bat317_liu_2020_o_4.22.20_148PM_LR.pdf.
[2] R. Schmuch et al., Nat. Energy 3 (2018) 267–278.
[3] D. Andre et al., J. Mater. Chem. A 3 (2015) 6709–6732.
[4] S.-T. Myung et al., ACS Energy Lett. 2 (2017) 196–223.
[5] H.H. Sun, ACS Energy Lett. 5 (2020) 1136–1146.
[6] Cobalt London Metal Exchange (2023). https://www.lme.com/en/Metals/EV/LME-Cobalt# (2023).
[7] K. Turcheniuk et al., Mater. Today 42 (2021) 57–72.
[8] C.B.L. Nkulu et al., Nat. Sustain. 1 (2018) 495–504.
[9] H.-H. Ryu et al., Energy Environ. Sci. 14 (2021) 844–852.
[10] M. Bianchini et al., Angew. Chem. Int. Ed. 58 (2019) 10434–10458.
[11] H.-H. Ryu et al., J. Mater. Chem. A 30 (2019) 1808–1814.
[12] U.-H. Kim et al., Energy Environ. Sci. 11 (2018) 1271–1279.
[13] C.S. Yoon et al., Chem. Mater. 30 (2018) 1808–1814.
[14] C.S. Yoon et al., ACS Energy Lett. 2 (2017) 1150–1155.
[15] C. Geng et al., Adv. Energy Mater. 12 (2021) 2103067.
[16] H.-J. Noh et al., J. Power Sources 233 (2013) 121–130.
[17] H.-H. Ryu et al., Chem. Mater. 30 (2018) 1155–1163.
[18] H. Kaneda et al., J. Mater. Chem. A 9 (2021) (1994) 21981–21982.
[19] D. Kitsche et al., Mat. Adv. 1 (2020) 639–647.
[20] L. Mu et al., ACS Appl. Mater. Interfaces 12 (2020) 12874–12882.
[21] F. Kong et al., Chem. Mater. 28 (2016) 6942–6952.
[22] L. Mu et al., Chem. Mater. 31 (2019) 9769–9776.
[23] T. Weigel et al., ACS Energy Lett. 4 (2019) 508–516.
[24] J. Chen et al., Front. Chem. 7 (2019) 1–10.
[25] C.S. Yoon et al., ACS Energy Lett. 3 (2018) 1634–1639.
[26] X. Xiong et al., J. Power Sources 245 (2014) 183–193.
[27] X. Xiong et al., J. Mater. Chem. A 2 (2014) 11691–11696.
[28] F. Riewald et al., J. Electrochem. Soc. 169 (2022) 020529.
[29] A. Liu et al., J. Electrochem. Soc. 168 (2021) 050506.
[30] W. Li et al., Adv. Mater. 32 (2020) 2002718.
[31] G.-T. Park et al., Mater. Today 52 (2022) 9–18.
[32] U.-H. Kim et al., Nat. Energy 5 (2020) 860–869.
[33] T. Nishimura et al., J. Mater. Chem. A 14 (1995) 1046–1047.
[34] E. Trevisanello et al., Adv. Energy Mater. 11 (2021) 2003400.
[35] H.-H. Ryu et al., ACS Energy Lett. 6 (2021) 2726–2734.
[36] N.-Y. Park et al., ACS Energy Lett. 7 (2022) 2362–2369.
[37] H.H. Sun et al., ACS Appl. Energy Mater. 2 (2019) 6002–6011.
[38] H.H. Sun et al., ACS Nano 14 (2020) 17142–17150.
[39] H.-H. Ryu et al., Mater. Today 36 (2020) 73–82.
[40] I.A. Ovid'ko et al., Acta Mater. 52 (2004) 1201–1209.
[41] G.-T. Park et al., Energy Environ. Sci. 14 (2021) 6616–6626.
[42] G.-T. Park et al., Energy Environ. Sci. 14 (2021) 5084–5095.
[43] C. Schwab et al., Phys. Chem. Chem. Phys. 21 (2019) 26066–26076.
[44] S. Yang et al., RSC Adv. 6 (2016) 94000–94009.
[45] M. Li et al., Science 367 (2020) 979–980.
[46] I. Nakai et al., J. Solid State Chem. 140 (1998) 145–148.
[47] A. Aishova et al., Adv. Energy Mater. 10 (2019) 1903179.
[48] H.-H. Ryu et al., Mater. Today 56 (2022) 8–15.
[49] Y.S. Meng et al., Chem. Mater. 17 (2005) 2386–2394.
[50] S. Hwang et al., Chem. Mater. 26 (2014) 1084–1092.
[51] K. Nam et al., Adv. Funct. Mater. 23 (2013) 1047–1063.
[52] U.-H. Kim et al., Mater. Today 23 (2019) 26–36.
[53] G.-T. Park et al., Nat. Energy 7 (2022) 946–954.
[54] T. Deng et al., Joule 3 (2019) 2550–2564.
[55] E. Markevich et al., ACS Appl. Energy Mater. 1 (2018) 2600–2607.
[56] H.-H. Ryu et al., ACS Energy Lett. 8 (2023) 1354–1361.